A Geometrically Frustrated Family of $M^{II}M^{III}F_5(H_2O)_2$ Mixed–Metal Fluorides with Complex Magnetic Interactions

Navindra Keerthisinghe, Anna A. Berseneva, Vladislav V. Klepov[†], Gregory Morrison, Hans-Conrad zur Loye[*]

Department of Chemistry and Biochemistry, University of South Carolina, Columbia, SC, 29208, United States

*Corresponding author. E-mail: zurloye@mailbox.sc.edu

[†]*currently at: Department of Chemistry, Northwestern University, Evanston, IL, 60208, United States*

Abstract

Inverse weberites are of interest as geometrically frustrated magnetic materials due to their unique cation arrangement. We have synthesized nine isostructural materials that adopt the inverse weberite crystal structure, which consists of cross-linked kagome layers. These materials, having the general formula $M^{II}M^{III}F_5(H_2O)_2$ (M^{II} = Co, Mn, Ni, and Zn; M^{III} = Ga, Cr, Fe, and V), were synthesized using mild hydrothermal conditions, which yielded phase pure samples after reaction conditions optimization. Their crystal structures, optical, thermal, and magnetic behavior were characterized using single crystal X-ray diffraction, UV-vis spectroscopy, thermogravimetric analysis, and by measuring the magnetic susceptibility and isothermal magnetization data respectively. Three distinct types of magnetism were observed including simple paramagnetism, antiferromagnetism and canted antiferromagnetism, the latter is accompanied with a high frustration index *f* in a range 4.16–8.09. We demonstrated that the magnetic behavior of inverse weberites depends on the presence or absence of unpaired electron containing cations on the two distinct crystallographic sites, which can be employed for the prediction of the magnetic properties of other compounds in this rich and diverse family.

Introduction

Magnetic frustration is typically observed and studied in select structure types that exhibit geometric frustration, including the pyrochlore, the hexagonal tungsten bronze, the weberite and the inverse weberite structures. The pyrochlore and weberite structure-types bear a relationship to the fluorite structure, AX_2, and are often described as anion deficient fluorite superstructures with compositions of $A_2B_2X_7$ for the pyrochlore and weberite structures, and $\square_2B_2X_5(H_2O)_2$ ($\square$ = vacancy) for the inverse weberite structure.[1–3] The pyrochlore and weberite structures exist as both oxides and fluorides, where the latter, $A_2B_2F_7$, have attracted attention recently due to the ability of the fluorides, for charge reasons, to accommodate late 3*d* transition elements, resulting in magnetic frustration as well as intriguing magnetic interactions in systems such as $NaCaCo_2F_7$, $NaSrMn_2F_7$ and $NaSrFe_2F_7$[4, 5] pyrochlores, and Na_2CoCrF_7, Na_2CoFeF_7,[6] Na_2NiFeF_7[7] and Na_2MnFeF_7[8] weberites.

Over the years, a large number of pyrochlore and weberite fluorides, $A_2B_2F_7$ have been synthesized and investigated for their extensive magnetic properties that are very sensitive to the specific magnetic and non-magnetic cations that make up the structures.[9] An extensive compilation of weberite fluoride compositions were published by Nino and coworkers[10] and frustrated magnetic pyrochlore fluoride compositions were reviewed by Reig-i-Plesis.[9] In addition, defect pyrochlore fluorites of the type $AB^{2+}B^{3+}F_6$, where a fluorine atom is missing and the A site is half-occupied compared to pyrochlore structure, such as $RbFe_2F_6$, $CsNiCrF_6$ and $CsMn_2F_6$, with and without crystallographically ordered transition metals, have been synthesized and studied.[11–14] A comprehensive review of inorganic fluorides was recently published by the Tressaud group.[15] By comparison with fluoride pyrochlores (~16) and weberites (~81), far fewer inverse weberite compositions (~13) have been reported to date,[10, 16] although they were studied for their magnetic frustration already in the 1970–1980's[1, 2, 17–20] and those known have been compiled.[10, 15]

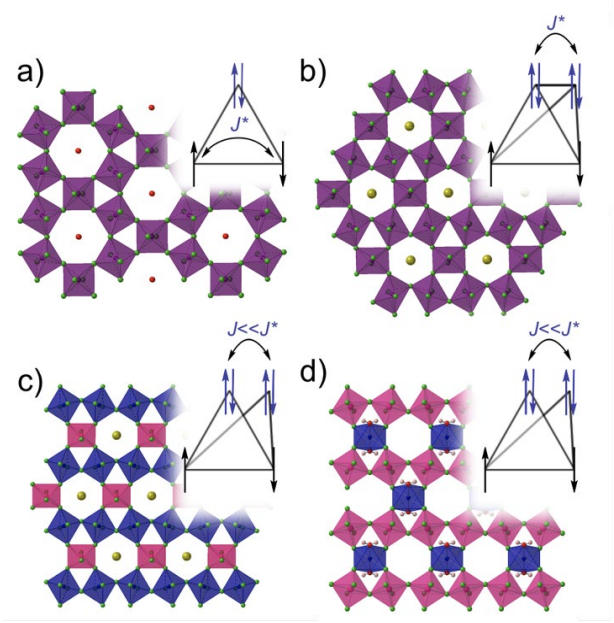

Figure 1. Individual kagome layer of (top left), hexagonal tungsten bronze[21] (BF_6 in purple octahedra, A cations in red sphere) (top right) pyrochlore[5] (BF_6 in purple octahedra, A cations in yellow spheres)[21] (bottom left) weberite[22] ($M^{II}F_6$ in blue octahedra, $M^{III}F_6$ in pink octahedra, A cations in yellow spheres) and (bottom right) inverse weberite ($M^{III}F_6$ in pink octahedra, $M^{II}F_4(H_2O)_2$ in blue octahedra). The insets show triangular plaquettes with frustrated spins.

The structural relationship between the fluorite, pyrochlore and weberite structures was recently reviewed.[10] In brief, both the pyrochlore and the weberite structures can be described as resulting from the stacking of AB_3 and A_3B layers where the different stacking of the layers results in the different coordination environments of the anions in the weberite and pyrochlore structures. (The AB_3 layer in the pyrochlore structure is often described as hexagonal tungsten bronze-related layer) An additional outcome of this stacking is the creation of a kagome type network for the A cations (Figure 1). This kagome arrangement is the origin of the observed magnetic frustration in these materials which is of interest for the unusual magnetic ground states and physical properties that are related to it.[23–30] Magnetic frustration occurs primarily from competing antiferromagnetic spin interactions caused by the topology of the lattice that hinders simultaneous antiferromagnetic arrangement of coupled magnetic moments, and the types of structures that exhibit magnetic frustration due to kagome-net arrangements include the weberite and pyrochlore[4, 9, 31–34] lattices. These structures mainly consist of triangular or tetrahedral arrangements that impose spin constraints that cause magnetic frustration. Experimentally, the degree of frustration of a material is often expressed as a deviation of the magnetic ordering

temperature from the Weiss constant in the form of the frustration index $f = |\Theta_{CW}|/T_C$, where Θ_{CW} is the Curie-Weiss temperature and T_C is magnetic ordering temperature.[24]

The kagome lattice is a planar array of corner-shared triangles and is considered one of the most magnetically frustrated structures. Compounds with kagome layer arrangements are highly sought after for their potential applications in generating novel spin liquids.[35–42] Different arrangements of kagome layers can lead to lattices exhibiting more complex frustration geometries. One example of such an arrangement is observed in weberites, where two kagome layers are cross-linked with each other at an almost 90° angle. The weberites have the general formula of $A_2M^{II}M^{III}F_7$ (A is an alkali metal, M^{II} and M^{III} are 3*d* metal cations), where both M^{II} and M^{III} cations are in distinct octahedral sites.[22, 43–46] In the weberite structure, the $M^{II}F_5$ chains of corner shared octahedra run along the *b*-axis and are connected to adjacent chains by $M^{III}F_6$ octahedra, resulting in $M^{II}M^{III}$ kagome layers. The two A cations, which reside in 7 and 8 coordinate environments, are located between the chains and charge balance the fluoride framework. Inverse weberites, which have the general formula $M^{II}M^{III}F_5(H_2O)_2$, are a variation on the weberite structure in which the most obvious difference is that the M^{II} and M^{III} octahedral sites are switched. Two additional important differences are the replacement of two F atoms by water molecules and the absence of A cations (Figure 2).[3, 47, 48] Both weberites and inverse weberites have been investigated to understand the concept of coupled magnetic frustration in compositions where two types of cations occupy distinct crystallographic sites.[6, 19, 20, 46, 49] In 1980s, Laligant *et al.* successfully synthesized $M^{II}Fe^{III}F_5(H_2O)_2$ (M^{II} = Fe, Mn, Co, Ni and Zn) using solvothermal methods and their studies indicate that in inverse weberites frustrated magnetism can be induced when both M^{II} and M^{III} have unpaired electrons.[1, 2, 17, 50–52] However, frustrated magnetism properties were studied only for Fe^{3+}-based compounds, and that of other inverse weberite structures has not been studied yet.

Herein, we report the mild hydrothermal synthesis[53–59] of nine isostructural inverse weberite fluoride hydrates (**1-9**) with the general formula $M^{II}M^{III}F_5(H_2O)_2$ (M^{II} = Co, Mn, Ni, and Zn; M^{III} = Ga, Cr, Fe, and V) and discuss their crystal structure, synthesis, thermal, optical, and magnetic behavior. Seven of the reported compositions (**1-5, 8** and **9**) are new and two other compositions (**6 and 7)** were reported previously.[50] The material syntheses involved two different reaction profiles, including thermal quenching techniques, to obtain the phase pure products. The crystal structures were determined by single crystal X-ray diffraction, thermal

properties were evaluated through thermogravimetric analysis as well as differential thermal analysis, optical properties were studied by UV-vis spectroscopy, and finally their magnetic behavior was analyzed by collecting magnetic susceptibility vs. temperature and magnetization vs. field data. Even though all the materials are isostructural, we observed three different types of magnetic behavior in these compounds, paramagnetism, antiferromagnetism and frustrated canted antiferromagnetism. Interestingly, we determined that based on the presence or absence of unpaired electrons in the M^{II} and M^{III} cations, the overall magnetic behavior changes and that this information can be used to predict the occurrence of magnetic frustration in the inverse weberite structures.

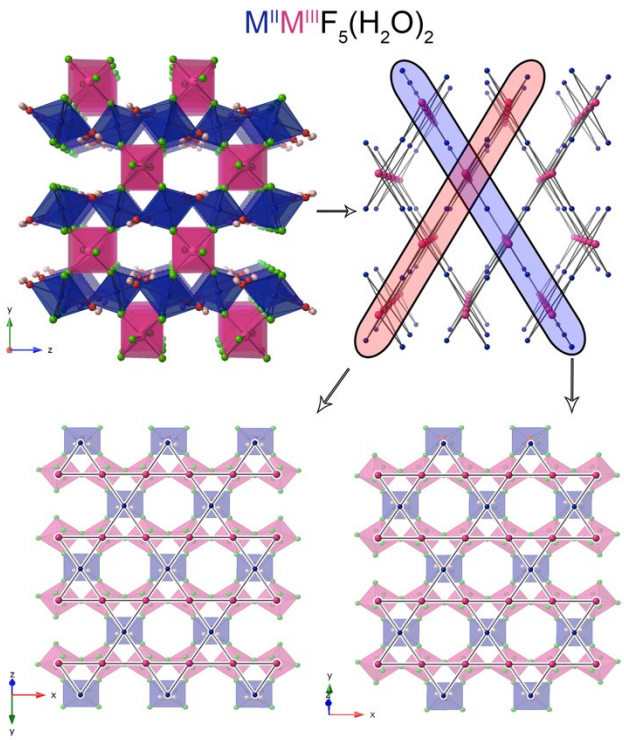

Figure 2. (top left) polyhedral representation of the 3D crystal structure of $M^{II}M^{III}F_5(H_2O)_2$ viewed along *a*-axis. Blue and pink octahedra represent $M^{II}F_4(H_2O)_2$ and $M^{III}F_6$, respectively. Red, green, and light-pink spheres represent O, F, and H atoms, respectively. (top right) Cation topology of the inverse weberite structure representing interconnected kagome layers. (bottom) Representations of the individual kagome layers. Blue and pink spheres represent $M^{II}F_4(H_2O)_2$ and $M^{III}F_6$ octahedra, respectively.

Experimental

Synthesis

The following materials were used as received without further purification: Ga_2O_3 (Alfa Aesar, 99.99%), V_2O_3 (Alfa Aesar, 95%), $Co(NO_3)_2 \cdot 6H_2O$ (Alfa Aesar, 98%), $Zn(NO_3)_2.6H_2O$ (Fisher Scientific), $Fe(NO_3)_3 \cdot 9H_2O$ (Alfa Aesar, 98%), FeF_3 (Strem Chemicals, 99+%), $CrCl_3 \cdot 6H_2O$ (MCB, 99%), $Mn(CH_3COO)_2 \cdot 4H_2O$ (Alfa Aesar, 98%), $Ni(CH_3COO)_2 \cdot 4H_2O$ (Sigma Aldrich, 98%), NiO (Alfa Aesar, 99%), $Co(CH_3COO)_2 \cdot 4H_2O$ (Alfa Aesar, 98%) and HF (48%, EMD).

Caution! HF is corrosive and acutely toxic. HF exposure causes severe burns that may not be immediately painful and may cause permanent injury or death. Appropriate personal protective equipment should be worn at all times when handling HF, and proper technique for using HF safely should always be followed. Temperature quenching of the hot reaction vessels in an ice bath may result in hot water splashing and proper precautions must be taken during this procedure (face shield, heat resistive laboratory coat, and thermally insulated gloves should be used).

The mild hydrothermal crystal growth technique was employed to synthesize all nine crystalline materials (**1-9**). The starting reagents were loaded into 23 mL PTFE liners using the quantities listed in Table 1 along with the indicated volumes of 48% HF. The PTFE liners were sealed inside stainless-steel autoclaves, which were placed inside a programmable oven. Two different temperature profiles were used to obtain phase pure products of the materials (**1-8**).

For **1-5** (compound numbers given according to Table 1), the oven was heated to 200 °C in an hour and allowed to dwell for 12 hours. After dwelling, the oven was shut off and allowed to cool to room temperature naturally. Similarly, for **6-8**, the oven was heated to 200 °C in an hour and allowed to dwell for 12 hours at which point the autoclaves were thermally quenched by placing them into an ice bath. For **9**, the oven was allowed to dwell at 200 °C for 36 hours and allowed to cool to room temperature at a cooling rate of 1 °C/min. Note that caution should be taken when opening the PTFE liners as it may contain HF vapor.

All reactions resulted in polycrystalline powders that were collected *via* vacuum filtration. The products **1-5, 9** were washed with acetone and allowed to air dry while products **6-8** were washed with water. Sufficiently large single crystals located among the polycrystalline powders were picked and used for single crystal X-ray diffraction and property measurements.

Any remnant fluoride ions were immobilized by treating the liquid waste with excess $CaCl_2$. A modified synthesis procedure that resulted in compound **10** can be found in the SI. It is included in Table 1 to illustrate the importance of the reagent choice when targeting the inverse weberites.

Table 1. Starting reagents for **1-10**

Chemical Formula	m(M^{II} source) (g)			m(M^{III} source) (g)				HF (ml)
	$M^{II}(CH_3COO)_2 \bullet 4H_2O$	$M^{II}(NO_3)_2 \bullet 6H_2O$	$M^{II}O$	$M^{III}{}_2O_3$	$M^{III}Cl_3 \bullet 6H_2O$	$M^{III}(NO_3)_3 \bullet 9H_2O$	MF_3	
$CoGaF_5(H_2O)_2$ **(1)**	0.1500			0.0451				1.8
$CoCrF_5(H_2O)_2$ **(2)**		0.1500			0.0549			1.8
$MnCrF_5(H_2O)_2$ **(3)**	0.1500				0.1305			1.8
$NiCrF_5(H_2O)_2$ **(4)**	0.1500				0.0642			1.8
$ZnCrF_5(H_2O)_2$ **(5)**		0.1500			0.0537			1.8
$CoFeF_5(H_2O)_2$ **(6)**		0.1500				0.1458		0.9
$NiFeF_5(H_2O)_2$ **(7)**	0.1500					0.1948		0.6
$NiVF_5(H_2O)_2$ **(8)**	0.1500			0.0587				0.5
$CoVF_5(H_2O)_2$ **(9)**	0.2490			0.1500				1.0
$NiFeF_5 \bullet 7H_2O$ **(10)**			0.1100				0.1116	2.0

Single-Crystal X-ray Diffraction (SXRD)

Single-crystal X-ray diffraction data were collected at 300(2)-303(2) K on a Bruker D8 QUEST diffractometer equipped with an Incoatec IμS 3.0 microfocus radiation source (MoKα, λ = 0.71073 Å) and a PHOTON II area detector. The crystals were mounted on a microloop using immersion oil. The raw data reduction and absorption corrections were performed using SAINT and SADABS programs.[60, 61] Initial structure solutions were obtained with SHELXTL-2017[62] using direct methods and Olex2 GUI.[63] Full-matrix least-square refinements against F were performed with SHELXL software.[64] The crystallographic data and results of the diffraction experiments are summarized in Table 2.

Table 2. Crystallographic data for **1-10.**

Chemical formula	**$CoGaF_5(H_2O)_2$ (1)**	**$CoCrF_5(H_2O)_2$ (2)**	**$MnCrF_5(H_2O)_2$ (3)**	**$NiCrF_5(H_2O)_2$ (4)**	**$ZnCrF_5(H_2O)_2$ (5)**	**$CoFeF_5(H_2O)_2$ (6)**	**$NiFeF_5(H_2O)_2$ (7)**	**$NiVF_5(H_2O)_2$ (8)**	**$CoVF_5(H_2O)_2$ (9)**	**$NiFeF_5{\cdot}7(H_2O)$ (10)**
Formula weight	259.68	241.96	237.97	241.74	248.40	245.81	245.59	240.68	240.90	160.78
Crystal shape, color	block, colorless	block, orange	block, green	needle, green	block, colorless	plank, colorless	plate, colorless	plank, orange	block, red	block, colorless
Crystal system	Orthorhombic									Triclinic
Space group, Z	Imma									$P\bar{1}$
a, Å	7.4003(2)	7.4078(2)	7.4651(4)	7.3323(3)	7.3765(2)	7.4874(4)	7.4227(2)	7.3983(2)	7.4913(3)	5.19300(10)
b, Å	10.5670(3)	10.6655(3)	10.8195(5)	10.6106(5)	10.6738(3)	10.7364(6)	10.6591(2)	10.6280(3)	10.7034(5)	5.2158(2)
c, Å	6.5491(2)	6.5611(2)	6.7317(3)	6.5499(3)	6.5792(2)	6.5663(6)	6.5529(10)	6.5556(2)	6.5613(3)	5.4473(2)
α, deg.	90									66.3620(0)
β, deg.	90									64.5300(10)
γ, deg.	90									84.0950(10)
V, $Å^3$	512.13(3)	518.38(3)	543.71(5)	509.58(4)	518.02(3)	527.85(5)	520.21(19)	515.46(3)	526.10(4)	121.596(7)
ρ_{calcd}, g/cm^3	3.368	3.100	2.907	3.151	3.185	3.093	3.136	3.101	3.041	2.196
Radiation (λ, Å)	MoKα, 0.71073									
μ, mm^{-1}	8.541	5.336	4.359	5.868	6.768	5.930	6.447	5.506	4.969	3.514
T, K	300(2) – 303(2)									
Crystal dim., mm^3	0.06×0.04×0.04	0.03×0.02×0.02	0.03×0.02×0.02	0.03×0.01×0.01	0.04×0.04×0.02	0.04×0.04×0.02	0.04×0.04×0.02	0.04×0.04×0.02	0.03×0.02×0.02	0.05×0.05×0.01
2θ range, deg.	4.16-36.28	3.65-32.48	3.56-30.33	3.66-36.36	3.64-36.39	3.64-34.90	3.81-36.30	3.65-36.34	7.614-56.554	8.56–56.536
Reflections collected	4016	11538	3390	3094	9667	4192	5946	3649	1306	8036
Data/restraints /parameters	363/0/33	521/0/32	390/0/31	337/0/32	340/0/32	345/0/32	341/0/33	339/0/32	359/0/30	599/0/70
R_{int}	0.0301	0.0338	0.0402	0.0352	0.0281	0.0369	0.0255	0.0287	0.0228	0.0434
Goodness of fit	1.165	1.046	1.197	1.244	1.051	1.158	1.162	1.136	1.168	1.220
$R_1(I > 2\sigma(I))$	0.0099	0.0175	0.0315	0.0258	0.0122	0.0414	0.0103	0.0127	0.0186	0.0193
wR_2 (all data)	0.0265	0.0403	0.0705	0.0594	0.0347	0.0776	0.0326	0.0295	0.0414	0.0520
Largest diff. peak/hole, $e{\cdot}Å^{-3}$	0.277/-0.261	0.395/-0.550	0.640/-0.819	0.663/-0.876	0.352/-0.255	1.139/-1.669	0.196/-0.206	0.220/-0.328	0.36/-0.30	0.34/–0.32

Powder X-ray Diffraction (PXRD)

Powder X-ray diffraction (PXRD) data were collected on ground polycrystalline samples to confirm phase purity (Figure S1). Data were collected on a Bruker D2 PHASER diffractometer using Cu Kα radiation over a 2θ range 5–65° with a step size of 0.02°.

Energy Dispersive Spectroscopy (EDS)

EDS was performed directly on crystals mounted on an SEM stub with carbon tape. Elemental analysis was done using a Tescan Vega-3 SEM instrument equipped with a Thermo EDS attachment (Table S1). The SEM was operated in low-vacuum mode with a 30 kV accelerating voltage and a 20 s accumulating time.

UV-vis Spectroscopy

UV-vis spectra were recorded using a Perkin-Elmer lambda 35 scanning spectrophotometer. The spectrophotometer was operated in diffuse reflectance mode and was equipped with an integrating sphere. Reflectance data were converted internally to absorbance via the Kubelka-Munk function.[65] Spectra were recorded in the 200–900 nm range.

Thermogravimetric Analysis

Thermogravimetric and differential thermal analysis (TGA/DTA) measurements were performed on polycrystalline powder samples using a SDT Q600 Thermogravimetric Analyzer and a platinum pan as the sample holder. Samples were heated from room temperature to the target temperature (600°C) at 10 °C/min under a flow of nitrogen gas (100 mL/min), and the resulting powders were analyzed by PXRD for phase identification post heating.

Magnetic Measurements

Susceptibility and magnetization measurements were performed using a Quantum Design MPMS3 SQUID magnetometer. Susceptibility measurements were performed under an applied field of 0.1 T in the temperature range of 2–300 K. Magnetization measurements were performed at 2 K in an applied field ranging from –5 T to 5 T. All magnetic data were corrected for radial offset and shape effects.[66]

Results and discussion

Synthesis

All the materials were grown as polycrystalline powders containing a small fraction of single crystals using mild hydrothermal syntheses with concentrated HF as an efficient fluorinating agent. The slow cooling profile yielded the desired products $M^{II}M^{III}F_5(H_2O)_2$ (M^{II} = Co, Mn, Ni, and Zn; M^{III} = Ga, and Cr) **1**–**5**. When this procedure was used to synthesize **6**–**8** $M^{II}M^{III}F_5(H_2O)_2$ (M^{II} =Co and Ni; M^{III} = Fe and V) it resulted in a mixture of the target phases **6**–**8** along with the previously reported $M^{II}M^{III}F_5$•7(H_2O) (M^{II} = Co and Ni; M^{III} = Fe and V) phases.[67] After multiple unsuccessful attempts to optimize the starting materials' molar ratios to crystallize the target phases **6**–**8**, we speculated that based on the high-water content of the side products $M^{II}M^{III}F_5$•7(H_2O) and their previously reported thermal decomposition to $M^{II}M^{III}F_5(H_2O)_2$,[67] higher temperatures would likely stabilize the dihydrate products, which can transform to the heptahydrate upon slow cooling (Table S3). To test this hypothesis, we employed a thermal quenching method and successfully isolated the desired compounds. Therefore, it is crucial to cool down the reaction vessels immediately after dwelling at 200 °C to isolate the $M^{II}M^{III}F_5(H_2O)_2$ phases. Nonetheless, a small amount of the $M^{II}M^{III}F_5(H_2O)_7$ phase was still present and only after washing with deionized water to selectively remove the heptahydrate phases was it possible to obtain phase pure $CoFeF_5(H_2O)_5$ (**6**) and $NiVF_5(H_2O)_5$ (**8**) as the final product. Even so, $NiFeF_5(H_2O)_2$ (**7**) was still mixed with a new heptahydrate polymorph, $NiFeF_5$•7H_2O (**10**). Details on the synthesis, structure determination and characterization of (**10**) can be found in the Supporting Information (SI, Figures S3 and S4). We were unable to obtain a phase pure sample of $NiFeF_5(H_2O)_2$ (**7**) and $CoVF_5(H_2O)_5$ (**9**) and, therefore, magnetism data for **7** and **9** were not collected.

Crystal Structure Description

Compounds **1-9** are isostructural and crystalize in the orthorhombic space group *Imma*. The structure of these materials is best described as an inverse weberite structure (Figure 2).[44] The M^{III} ions form $M^{III}F_6$ octahedra that share their trans-corners to build chains running along the [100] direction and these chains are linked by isolated $M^{II}F_4(H_2O)_2$ octahedra (Figure S2). The four fluorine atoms of $M^{II}F_4(H_2O)_2$ are located in the equatorial plane and are shared with four adjacent $M^{III}F_6$ octahedra, while the two water molecules are located in the axial positions

and function as terminal groups.[47] This linking of $M^{III}F_5$ octahedral chains by isolated $M^{II}F_4(H_2O)_2$ octahedra leads to an extended triangular framework as illustrated in Figure 2. The $M^{III}F_6$ octahedra in all compounds contain axial M^{III}–F1 bonds (1.918 – 1.955 Å) that are slightly elongated relative to the equatorial M^{III}–F2 bonds (1.870 – 1.915 Å), as they corner share *via* the axial fluorine atoms. Similarly, in the $M^{II}F_4(H_2O)_2$ octahedra, the M^{II}–O bonds (2.024 Å in $NiVF_5(H_2O)_2$) are slightly longer than the M^{II}–F2 bonds (2.007 Å in $NiVF_5(H_2O)_2$); the exceptions are the cobalt containing compositions **1**, **2**, **6** and **9**, where it is reversed. A listing of all bond lengths and bond angles for all materials **1-9** is given in Table S2.

UV-vis Spectroscopy

The studied compositions of inverse weberite have diverse optical properties resulting from different *d–d* transitions. Depending on the specific 3*d* metal, crystals can be light pink (**1** and **6**), green (**3**–**5**, **7**), orange (**2**), red (**9**), and brown (**8**). It is important to note that the single crystals may look almost colorless (Table 2), however the bulk materials will exhibit the listed colors. The variety of 3*d* metals probed in these studies include $V^{3+}(d^2)$, $Cr^{3+}(d^3)$, $Mn^{2+}(d^5)$, $Fe^{3+}(d^5)$, $Co^{2+}(d^7)$, $Ni^{2+}(d^8)$, and $Zn^{2+}(d^{10})$. While Zn^{2+} as well as Ga^{3+} are not optically active due to d^{10}-configuration, there also are no spin-allowed *d–d* transitions for high spin Mn^{2+} and Fe^{3+} due to high spin d^5-configuration. Since both metals in the inverse weberite structure are in octahedral environments, Tanabe-Sugano diagrams are useful for assigning absorption bands for $V^{3+}(d^2)$, $Cr^{3+}(d^3)$, $Co^{2+}(d^7)$, and $Ni^{2+}(d^8)$.[68–71] Band identification for Cr^{3+}, Co^{2+}, and Ni^{2+} used $ZnCrF_5(H_2O)_2$ (**5**), $CoGaF_5(H_2O)_2$ (**1**), and $NiFeF_5(H_2O)_2$ (**7**), respectively, as references.[72–74] For V^{3+}, band assignments were made based only on literature examples.[72–74] Figure 3 contains all the UV-vis spectra, and Table S4 includes details on absorption band locations as well as band assignments (Note only spin-allowed transitions were identified).

All Cr^{3+}-containing materials demonstrated absorption peaks at ~670, ~430, and ~300 nm. The Tanabe-Sugano diagram for d^3 suggested that these are $^4A_{2g} \rightarrow {}^4T_{1g}(P)$, $^4A_{2g} \rightarrow {}^4T_{1g}$, and $^4A_{2g} \rightarrow {}^4T_{2g}$ transitions, respectively. Using the Tanabe-Sugano diagram for d^3, the crystal field for $ZnCrF_5(H_2O)_2$ (**5**) was estimated as ~15,000 cm^{-1} (~1.86 eV) which is in line with the reported Cr^{3+}-activated fluoride phosphors.[75] For Co^{2+}- and Ni^{2+}-based materials only two absorption bands originating from *d–d* transitions fall into the visible region, while low-energy $^4T_{1g} \rightarrow {}^4T_{2g}$ (Co^{2+}) and $^3A_{2g} \rightarrow {}^3T_{2g}$ (Ni^{2+}) transitions lie in Near-IR, and hence could not be

observed with the available instrumentation. The typical Co-containing inverse weberite exhibits $^4T_{1g} \rightarrow {}^4A_{2g}$ (670–700 nm) and $^4T_{1g} \rightarrow {}^4T_{2g}$ (~505 nm) bands. Even though it is challenging to assign absorption bands for compounds with multiple absorbing ions, band identification for Ni^{2+} were performed on $NiFeF_5(H_2O)_2$ (**7**), where high-spin Fe^{3+} possesses no spin-allowed *d–d* transitions. Therefore, absorption peak maxima at ~740 nm and ~410 nm were assigned as $^3A_{2g} \rightarrow {}^3T_{1g}(F)$ and $^3A_{2g} \rightarrow {}^3T_{1g}(P)$ transitions, respectively. Our previous report for $[Ni(H_2O)_6]_2[MnF_6][MnF_4(H_2O)_2]$, $[Ni(H_2O)_6][CrF_5(H_2O)]_3$, $[Ni(H_2O)_6][FeF_5(H_2O)]_4$, and $[Ni(H_2O)_6][VOF_4(H_2O)]$ compositions[56] demonstrated that the bands corresponding to Ni^{2+} *d–d* transitions lie at ~700 nm and ~400 nm, respectively. Taking into account that previously reported fluorides contained $[Ni(H_2O)_6]^{2+}$ octahedra and that in the inverse weberite structure the Ni^{2+} coordination environment is $[NiF_4(H_2O)_2]^{2-}$, the slight decrease in transition energies is in line with the weaker crystal field of the F^- ligands compared to H_2O. Band assignment for V^{3+} were performed based on the literature example of $K_3V^{3+}F_6$ where $^3T_{1g} \rightarrow {}^3T_{2g}(F)$ and $^3T_{1g} \rightarrow {}^3T_{1g}(F)$ transitions were found. In $NiVF_5(H_2O)_2$ (**8**) the peak at ~740 nm was assigned as $^3T_{1g} \rightarrow {}^3T_{2g}(F)$ and the absorption band at ~460 nm was attributed to $^3T_{1g} \rightarrow {}^3T_{1g}(F)$. Therefore, UV-vis spectroscopy confirmed the presence of $V^{3+}(d^2)$, $Cr^{3+}(d^3)$, $Co^{2+}(d^7)$, and $Ni^{2+}(d^8)$ in **1**–**8**. At the same time, the inverse weberite compositions demonstrated a tunability of optical profiles due to the variety of 3*d* metals that can be integrated into the structure, which may be of interest in optics.

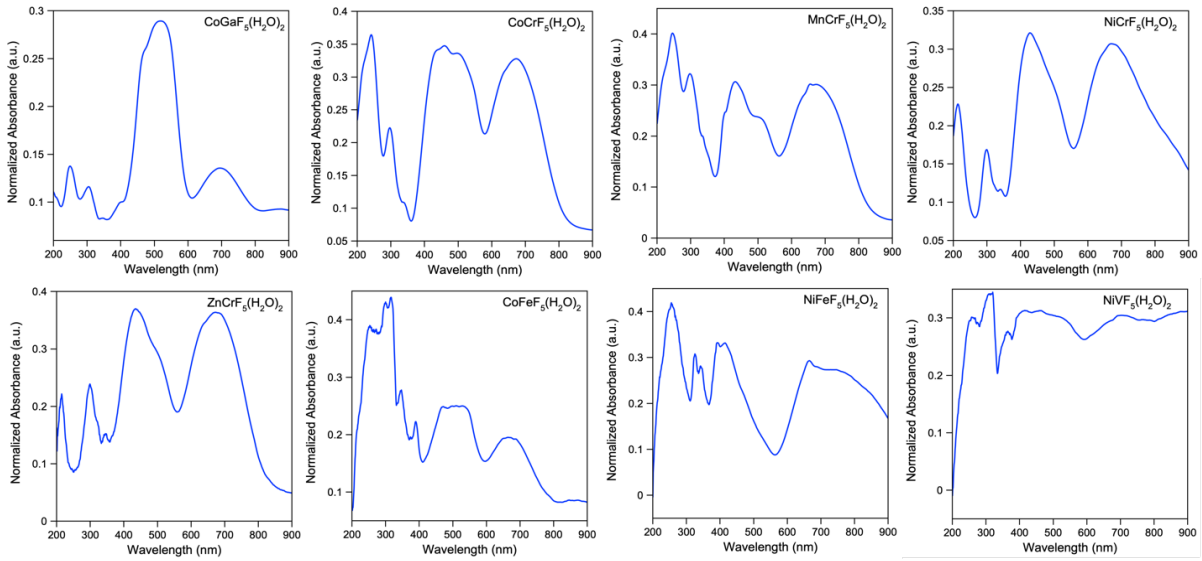

Figure 3. The solid-state UV/visible spectra for materials **1-8** (in order from left to right).

Thermogravimetric Analysis

Thermal properties of **1-8** were explored to study the structural stability of inverse weberites upon heating (Figures S5–S12). All materials exhibit a small weight loss at ~100 °C followed by one or two-step weight losses from 200 – 600 °C, leading to decomposition of the material. The post TGA products were analyzed by PXRD and the results are summarized in Table S5. The initial weight loss at ~100 °C can be attributed to the loss of surface water. The post TGA products for **1-8**, mostly consist of binary fluorides of the two metal cations along with an amorphous oxide, oxyfluoride or a ternary fluoride.

A previous report on the thermal dehydration of the inverse weberite $MgAlF_5(H_2O)_2$ indicates that heating above 300 °C results in the formation of the ternary fluoride $MgAlF_5$, which consist of trans-corner sharing $[AlF_5]$ octahedral chains and $[MgF_6]$ edge sharing octahedral chains that are connected via common F atoms. Upon further heating, beyond 500 °C the material fully decomposes to binary fluorides.[48] These results agree well with what is observed for **3** where a two-step decomposition results in the formation of MnF_2 and $CrMnF_5$. For the remaining compositions, (**1,2 and 4-8**), the competing processes that result in the loss of either HF or H_2O during heating readily cause the collapse of the inverse weberite framework and results in the formation of amorphous oxides or oxyfluorides as thermal decomposition products.

Magnetic Properties

Since the inverse weberite structure exhibits a triangular frustrated lattice, we studied the magnetic properties of the title compounds by measuring the temperature dependence of the magnetic susceptibility and magnetization vs field (MvH) data. The observed magnetic behavior of the title compounds is summarized in Table 3, listing the magnetic moments derived from Curie-Weiss fits (Figures 4 and 5), Weiss temperatures, transition temperatures, and frustration indices $f = |\Theta_{CW}|/T_c$, which indicate the degree of frustration in the samples. A slight difference between observed and calculated effective magnetic moments can be noticed for the Co-containing compositions **1**, **2** and **6**, likely due to contributions from spin-orbit coupling.[9]

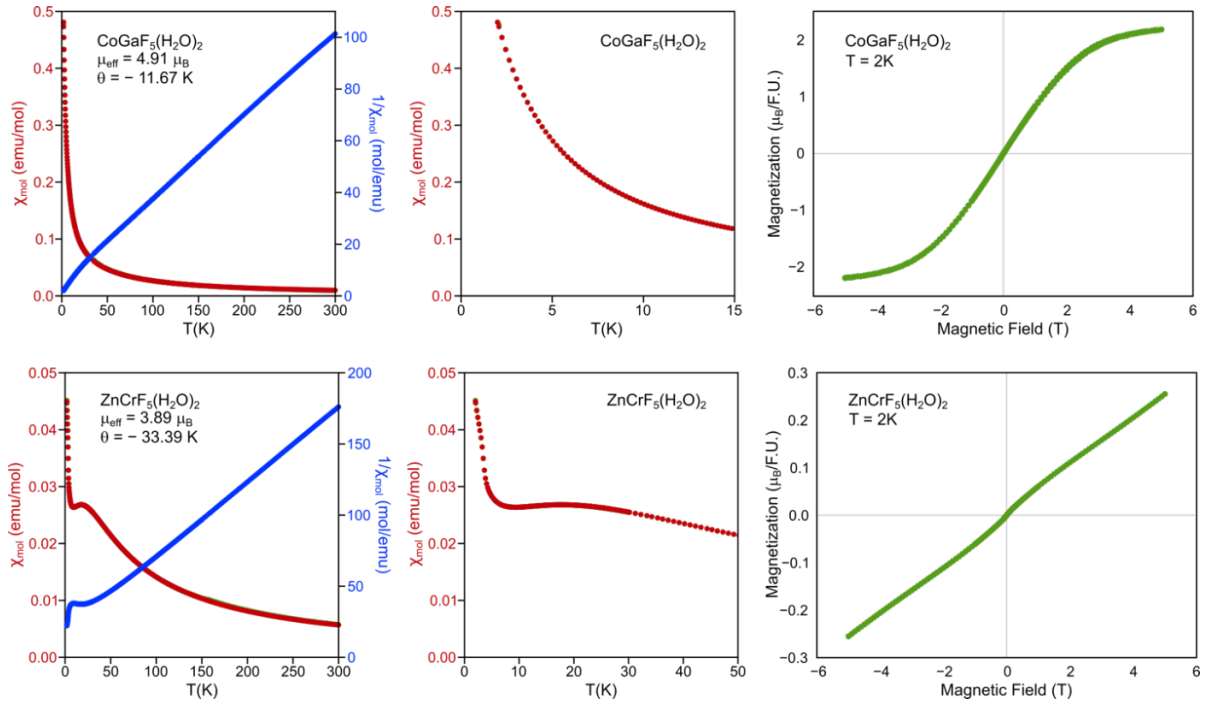

Figure 4. Magnetism data for materials **1** and **5**: (left) magnetic susceptibility and inverse magnetic susceptibility for the temperature range 2–300 K, (middle) magnetic susceptibility near the transition temperature, and (right) MvH plot at 2 K. Full scale magnetism plots for each material are provided in the SI (Figures S14–S16 and S26–S28). Zero-field cooled data shown in red, field-cooled data shown in green.

The magnetic behavior of these phases is strongly dependent on the specific cations on the M^{II} and M^{III} sites, which are connected into a corner-shared equilateral triangle to form kagome layers (Figure 2). This cation network leads to interconnected layers that each, individually, exhibits magnetic frustration, the degree of which is determined by the specific cations present in the layers. The type of magnetism exhibited ranges from diamagnetic, if neither M^{II} and M^{III} have any unpaired electrons, to paramagnetic if only M^{II} has unpaired electrons, to antiferromagnetic if only M^{III} has unpaired electrons, to frustrated canted antiferromagnetic when both M^{II} and M^{III} have unpaired electrons (Figure 6). Since the M^{II} cations are separated by $M^{III}F_5$ chains in the structure, compounds with diamagnetic M^{III} cations exhibit a paramagnetic behavior down to 2 K, e.g., $CoGaF_5(H_2O)_2$ (**1**). On the other hand, if $M^{III}F_5$ chains are separated by diamagnetic M^{II} cation, such as in $ZnCrF_5(H_2O)_2$ (**5**), antiferromagnetic interactions within the chains result in an antiferromagnetic transition in the sample at low temperatures ($T_N \approx 15.5$ K), which is accompanied by a significant drop in the

magnetic susceptibility. Negative Θ_{CW} (–33.39 K) derived from the Curie-Weiss law corroborates the antiferromagnetic interaction between Cr^{3+} ions which is in line the Kanamori-Goodenough rules for d^3-configuration.[76] Moreover, the previous investigation of the inverse weberite $ZnFeF_5(H_2O)_2$ magnetic structure demonstrated antiferromagnetic ordering of Fe^{3+} with an exact 180° between the spins ($T_N \approx 9$ K).[18]

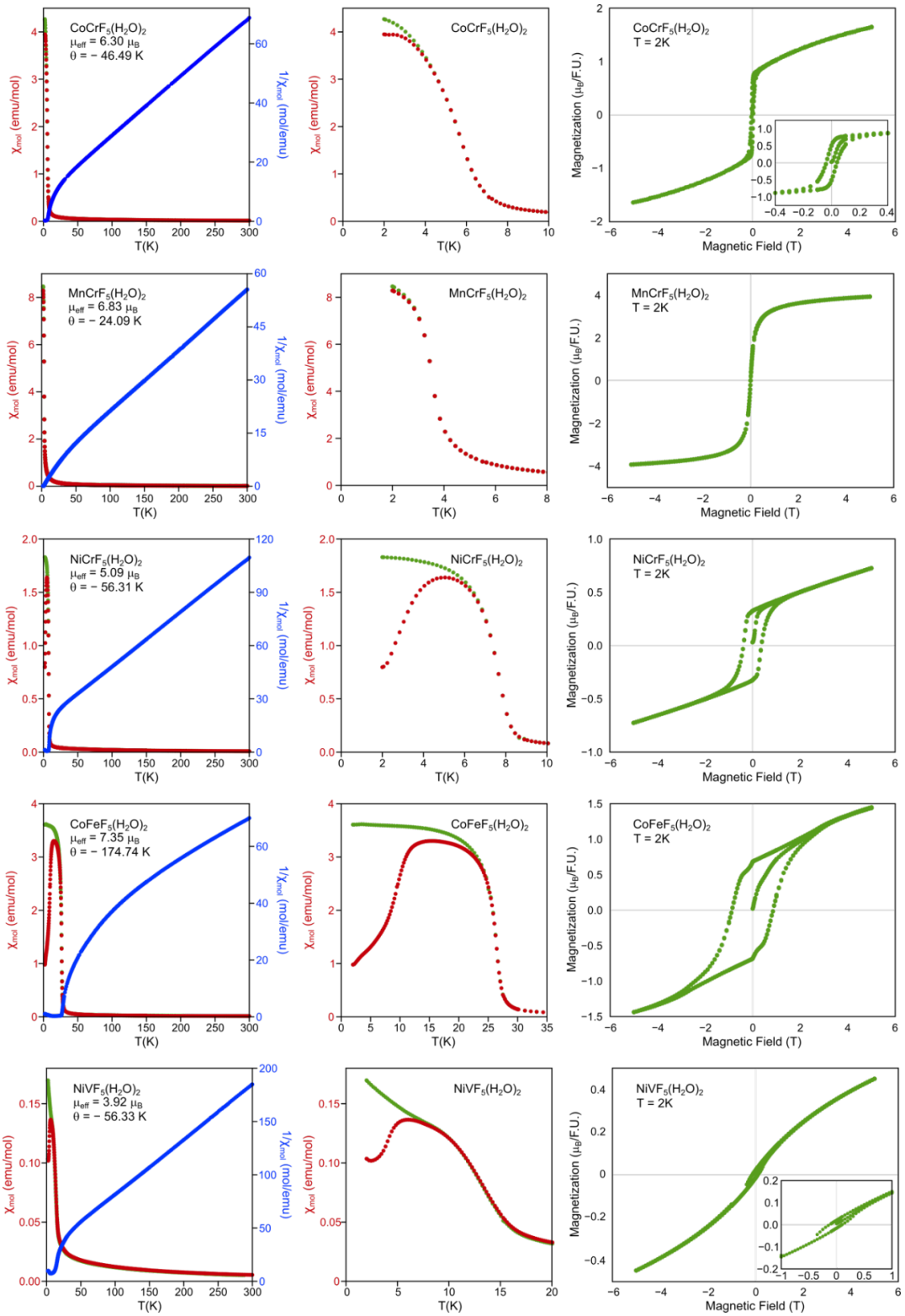

Figure 5. Magnetism data for materials **2-4, 6** and **8**: (left) magnetic susceptibility and inverse magnetic susceptibility for the temperature range 2–300 K, (middle) magnetic susceptibility near the transition temperature, and (right) MvH plot at 2 K. Full scale magnetism plots for each material are provided in the SI (Figures S17–S25 and S29–S34).

The magnetism data indicate that ideal antiferromagnetic ordering in the chains can be disrupted by introducing magnetically active cations on the M^{II} site, resulting in canted antiferromagnetic (or less likely ferrimagnetic) transitions in $M^{II}M^{III}F_5(H_2O)_2$ (M^{II} = Co, Mn, and Ni; M^{III} = Cr, Fe, and V) at low temperatures (3.5–26.4 K, Figure 5). Antiferromagnetic interaction between spins for those compositions is supported by negative Weiss values (Θ_{CW}) (Table 3). Moreover, the discrepancy between zero-field cooled and field cooled magnetic susceptibilities is indicative of interactions between canted spins (or less likely ferrimagnetic ordering, Figure 5). Finally, all $M^{II}M^{III}F_5(H_2O)_2$ compounds with two magnetically active cations except $MnCrF_5(H_2O)_2$ (**3**) exhibit a hysteresis loop, where the magnetization per formula unit (F.U.) after saturation is smaller than the value expected for ferrimagnetic ordering (Figure 5). For $MnCrF_5(H_2O)_2$ (**3**) the transition temperature is comparably low (≈ 3.5 K) and hence a hysteresis loop does not appear in the MvH plot collected at 2 K. Therefore, MvH data further provides an argument in favor of canted antiferromagnetic *vs* ferrimagnetic transition. Along the same lines, the reported magnetic structures of the related inverse weberites $M^{II}FeF_5(H_2O)_2$ (M = Mn and Fe) showed the presence of canted antiferromagnetic interactions. For instance, in $MnFeF_5(H_2O)_2$, Fe^{3+} spins within the FeF_5 chain are strongly canted resulted in 115.7° between the spins. Similarly, spins of Mn^{2+} and Fe^{3+} in Fe–Mn–Fe triangles cannot preserve pure antiferromagnetic interactions and, as a result, are canted with 102.8° and 140.2° between the spins. In future investigations, the magnetic structures of the reported canted antiferromagnets will be investigated by neutron diffraction studies to establish the actual magnetic structures.

Comparably high frustration indices (Table 3) for the $M^{II}M^{III}F_5(H_2O)_2$ (M^{II} = Co, Mn, and Ni; M^{III} = Cr, Fe, and V) materials highlight a significant role of frustration in achieving the ordered magnetic state. Interestingly, Cr-containing compounds (**2-4**) and $CoFeF_5(H_2O)_2$ show much higher frustration, in the range of 6.80 to 8.09, in comparison to $NiVF_5(H_2O)_2$ with $|f|$ equal to 4.16 (Table 3). We also estimated frustration indices for known inverse weberite compositions, e.g. for $MnFeF_5(H_2O)_2$ and $Fe_2F_5(H_2O)_2$ $|f|$ equal to 6.76 and 5.28, respectively.[1, 2, 18, 51] Fe^{3+}-containing compositions show frustration in the range of 5.28 to 6.76 which is overall lower than that found for Cr^{3+}-based compounds. Interestingly, the highest frustration indices for Cr^{3+}- and Fe^{3+} compounds were observed for the compositions with the same number of unpaired electrons, e.g. in $CoCrF_5(H_2O)_2$ (**2**) Co^{2+} and Cr^{3+} have 3 unpaired electrons and in $MnFeF_5(H_2O)_2$ Mn^{2+} and Fe^{3+} have 5 unpaired electrons. Moreover, we estimated frustration

indices for two known weberites Na_2CoCrF_7 and Na_2CoFeF_7,[6] where in contrast to the inverse weberite compounds, $M^{II}F_6$ octahedra form chains. Interestingly, the inverse weberite compounds have higher frustration indices than analogous weberite compounds, e. g. $|f|$ equal to 6.63 and 1.25 for $CoFeF_5(H_2O)_2$ (**6**) and Na_2CoFeF_7,[6] respectively. At the same time Na_2CoCrF_7, which contains Cr^{3+}, demonstrated a fairly high $|f|$ (7.27),[6] however, it is still lower than that for $CoCrF_5(H_2O)_2$ (**2**). More compounds of this family need to be synthesized to draw a definitive conclusion on the impact of the M^{III} cation on the overall frustration. In general it seems that the inverse weberite structures demonstrated frustrated indices that are lower than those for pyrochlore antiferromagnets with $|f|$ of 19 to 58.[5, 33, 77, 78] Presumably, this trend can be explained by the arrangement of the kagome layers in the crystal structures. For $A_2B_2X_7$ pyrochlore structures each B cation belongs to three kagome layers, while for inverse weberite structures each M^{II} and M^{III} cation are a part of one and two kagome layers, respectively (Figure 1). One can expect a decrease in the frustration index going from the pyrochlore to the weberite and the inverse weberite and finally to the hexagonal tungsten bronze (only one kagome layer for B cations, Figure 1). For example, for Mn^{2+}- and Fe^{3+}-containing fluorides with d^5-configuration, the frustration indices are 36, 6.76, and 6.18 for the $NaSrMn_2F_7$ pyrochlore, the $MnFeF_5(H_2O)_2$ inverse weberite, and the hexagonal tungsten bronze FeF_3, respectively. This supports that the pyrochlore structure type is the most geometrically frustrated system among the series of these three structure types.

These studies are consistent with previous studies of inverse weberite systems. Specifically, previous studies on the $M^{II}FeF_5(H_2O)_2$ (M^{II} = Fe, Mn, and Zn) system by Ferey *et al.* have indicated that the $Fe^{III}F_5$ octahedral chains in $ZnFeF_5(H_2O)_2$ exhibit long range antiferromagnetic behavior, which changes when Zn^{2+} is replaced by a paramagnetic M^{II} cation that introduces magnetic frustration to the system.[1, 50, 79] Overall, the observed trends support the idea of frustration being induced by the M^{II} cations onto the antiferromagnetic chains of M^{III} cations leads to a frustrated canted antiferromagnetic system.

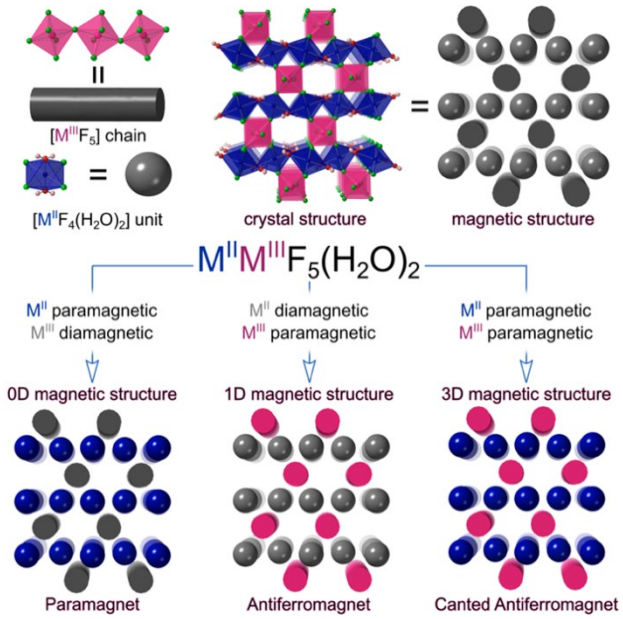

Figure 6. Schematic representation of the changes in magnetic behavior and magnetic structure dimensionality in inverse weberites as a function of unpaired electrons in the M^{II} and M^{III} cations.

Table 3. Magnetic properties of **1-8**

	M^{II}	**M^{III}**	**Magnetic properties**	**Effective magnetic moment (μ_{eff}) (μ_B/F.U.)**		**Θ_{CW} (K)**	**Magnetic ordering T (K)**	**Frustration Index**
				observed	calculated			
1	Co	Ga	Paramagnetic	4.91	3.87	–11.67	–	–
2	Co	Cr	Canted antiferromagnetic	6.30	5.47	–46.49	5.74	8.09
3	Mn		Canted antiferromagnetic	6.83	7.07	–24.09	3.54	6.80
4	Ni		Canted antiferromagnetic	5.09	4.79	–56.31	7.75	7.27
5	Zn		Antiferromagnetic	3.89	3.87	–33.39	15.55	2.31
6	Co	Fe	Canted antiferromagnetic	7.35	6.24	–174.74	26.35	6.63
8	Ni	V	Canted antiferromagnetic	3.92	4.00	–56.33	13.55	4.16

Conclusion

Inverse weberites are a class of magnetically frustrated compounds whose structure can be described as resulting from the intersection of two kagome lattices, where each M^{II} and M^{III} magnetic ion induces frustration in one and two kagome layers, respectively. In this report we described the synthesis, structural, optical, and magnetic characterization of nine isostructural compounds with the general formula $M^{II}M^{III}F_5(H_2O)_2$. Stabilization of these phases under hydrothermal synthesis conditions can be achieved by either slow cooling for $M^{II}M^{III}F_5(H_2O)_2$ (M^{II} = Co, Mn, Ni, and Zn; M^{III} = Ga and Cr) or by thermal quenching for $M^{II}M^{III}F_5(H_2O)_2$ (M^{II} =Co and Ni; M^{III} = Fe and V), which indicates subtle changes in their thermodynamic stability as a function of temperature. Thermal properties studied by TGA/DTA demonstrated the stability of inverse weberites up to 200–250 °C followed by decomposition of pristine materials to metal fluorides and oxides. The optical properties of phase pure materials were studied and typical *d–d* transitions were observed in the absorbance plots, demonstrating the tunability of the optical behavior as a function of the 3*d* metal.

The magnetism of $M^{II}M^{III}F_5(H_2O)_2$ is dominated by antiferromagnetic interactions in the $M^{III}F_5$ chains, which can be disrupted by interchain M^{II} cations to induce canted antiferromagnetic ordering in the magnetic structure. For example, magnetic susceptibility measurements on $ZnCrF_5(H_2O)_2$ with $Cr^{3+}F_5$ magnetic chains exhibited antiferromagnetic ordering at 15.5 K, while $CoGaF_5(H_2O)_2$ with non-magnetic Ga^{3+} exhibits no magnetic transitions down to 2 K. All compositions with magnetic M^{II} and M^{III} cations show canted antiferromagnetic behavior, with frustration indices varying from 4.16 for $NiVF_5(H_2O)_2$, to the 5.28–6.76 range for Fe^{3+}-containing compositions and finally to the 6.80–8.09 range for Cr^{3+}-based compositions. Future investigations of these magnetic structures via neutron diffraction is likely to shed light on the impact of the M^{III} cation on the overall frustration.

Acknowledgements

Financial support for this work was provided by the National Science Foundation under DMR-1806279 and is gratefully acknowledged.

Supporting Information
The Supporting Information is available free of charge at ???

Synthesis and characterization of $NiFeF_5 \cdot 7H_2O$ (**10**), powder X-ray diffraction patterns, elemental composition data, bond length and bond angle data, UV/visible absorption band assignments, TGA data, magnetic data plots.

Accession Codes

CCDC 2081079-2081081, 2081084-2081086, 2081151, 2081303 and 2091356 contain the supplementary crystallographic data for this paper. These data can be obtained free of charge via www.ccdc.cam.ac.uk/data_request/cif, or by emailing data_request@ccdc.cam.ac.uk, or by contacting The Cambridge Crystallographic Data Centre, 12 Union Road, Cambridge CB2 1EZ, UK; fax: +44 1223 336033.

References

(1) Laligant, Y.; Calage, Y.; Torres-Tapia, E.; Greneche, J. M.; Varret, F.; Ferey, G. Crystal Structure of the Inverse Weberite $ZnFeF_5(H_2O)_2$, Magnetic and Mössbauer Study of the Antiferromagnet $ZnFeF_5(H_2O)_2$ and Ferrimagnet $MnFeF_5(H_2O)_2$. *J. Magn. Magn. Mater.* **1986**, *61*, 283-90.

(2) Laligant, Y.; Leblanc, M.; Pannetier, J.; Ferey, G. Ordered Magnetic Frustration. IV. The Two Magnetic Structures of the Inverse Weberite $Fe_2F_5(H_2O)_2$: an Example of the Thermal Evolution of the Frustration Character. *J. phys., C, Solid state phys.* **1986**, *19*, 1081-95.

(3) Subramanian, M. A.; Marshall, W. J.; Hoffmann, R.-D.; Sleight, A. W. Synthesis and Structure of Some M^{II}/M^{III} Mixed Fluorides with Pyrochlore and Weberite Related Structures. *Z. Naturforsch. Sect. B* **2006**, *61*, 808-12.

(4) Krizan, J. W.; Cava, R. J. $NaCaCo_2F_7$: A Single-Crystal High-Temperature Pyrochlore Antiferromagnet. *Phys. Rev. B* **2014**, *89*, 214401.

(5) Sanders, M. B.; Krizan, J. W.; Plumb, K. W.; McQueen, T. M.; Cava, R. J. $NaSrMn_2F_7$, $NaCaFe_2F_7$, and $NaSrFe_2F_7$: Novel Single Crystal Pyrochlore Antiferromagnets. *Journal of Physics: Condensed Matter* **2017**, *29*, 045801.

(6) Boireau, A.; Gravereau, P.; Dance, J. M.; Tressaud, A.; Hagenmuller, P.; Soubeyroux, J. L.; Welsch, M.; Babel, D. Structural and Magnetic Properties of Several Cobalt (II) Weberites. *Mater. Res. Bull.* **1993**, *28*, 27-38.

(7) Heger, G.; Viebahn-Hänsler, R. The magnetic structure of Na_2NiFeF_7. *Solid State Commun.* **1972**, *11*, 1119-22.

(8) Holler, H.; Babel, D.; Samouël, M.; de Kozak, A. The Crystal Structure of Barium Manganese(II) Iron(III) Fluoride $BaMnFeF_7$. *J. Solid State Chem.* **1981**, *39*, 345-50.

(9) Reig-i-Plessis, D.; Hallas, A. M. Frustrated Magnetism in Fluoride and Chalcogenide Pyrochlore Lattice Materials. *Phys. Rev. Mater.* **2021**, *5*, 030301.

(10) Cai, L.; Nino, J. C. Complex Ceramic Structures. I. Weberites. *Acta Crystallogr., Sect. B: Struct. Sci.* **2009**, *65*, 269-90.

(11) Banks, E.; Deluca, J. A.; Berkooz, O. Preparation, Magnetic Properties and Mossbauer Study of the Modified Pyrochlores $M^{II}M^{III}F_6A$. *J. Solid State Chem.* **1973**, *6*, 569-73.

(12) Kim, S. W.; Kim, S.-H.; Halasyamani, P. S.; Green, M. A.; Bhatti, K. P.; Leighton, C.; Das, H.; Fennie, C. J. $RbFe^{2+}Fe^{3+}F_6$: Synthesis, Structure, and Characterization of a New Charge-Ordered Magnetically Frustrated Pyrochlore-Related Mixed-Metal Fluoride. *Chem. Sci.* **2012**, *3*, 741-51.

(13) Klepov, V. V.; Pace, K. A.; Berseneva, A. A.; Felder, J. B.; Calder, S.; Morrison, G.; Zhang, Q.; Kirkham, M. J.; Parker, D. S.; zur Loye, H.-C. Chloride Reduction of Mn^{3+} in Mild Hydrothermal Synthesis of a Charge Ordered Defect Pyrochlore, $CsMn^{2+}Mn^{3+}F_6$, a Canted Antiferromagnet with a Hard Ferromagnetic Component. *J. Am. Chem. Soc.* **2021**, *143*, 11554-67.

(14) Zinkin, M. P.; Harris, M. J.; Zeiske, T. Short-range Magnetic Order in the Frustrated Pyrochlore Antiferromagnet $CsNiCrF_6$. *Phys. Rev. B* **1997**, *56*, 11786-90.

(15) Leblanc, M.; Maisonneuve, V.; Tressaud, A. Crystal Chemistry and Selected Physical Properties of Inorganic Fluorides and Oxide-Fluorides. *Chem. Rev.* **2015**, *115*, 1191-254.

(16) Hellenbrandt, M. The Inorganic Crystal Structure Database (ICSD)—Present and Future. *Crystallogr. Rev.* **2004**, *10*, 17-22.

(17) Laligant, Y.; Pannetier, J.; Labbe, P.; Ferey, G. A New Refinement of the Crystal Structure of the Inverse Weberite $Fe_2F_5(H_2O)_2$. *J. Solid State Chem.* **1986**, *62*, 274-7.
(18) Laligant, Y.; Pannetier, J.; Ferey, G. Ordered Magnetic Frustration. VI. Crystal and Magnetic Structures of the Inverse Weberites $ZnFeF_5(H_2O)_2$ and $MnFeF_5(H_2O)_2$ at 1.5K from Powder Neutrin Diffraction. *J. Solid State Chem.* **1987**, *66*, 242-50.
(19) Laligant, Y.; Ferey, G.; Heger, G.; Pannetier, J. Ordered Magnetic Frustration. XI. Refinement of the Crystal and Frustrated Magnetic Structures of the Direct Weberite Na_2NiCrF_7 by Neutron Powder Diffraction. *Z. Anorg. Allg. Chem* **1987**, *553*, 163-71.
(20) Albino, M.; Clark, L.; Lhoste, J.; Payen, C.; Grenèche, J. M.; Lightfoot, P.; Maisonneuve, V.; Leblanc, M. A magnetisation and Mössbauer study of Triazole $(M_{1-x}^{2+}M_x^{3+})M^{3+}F_5(Htaz)_{1-x}(taz)_x$ Weberites (M = Fe, Co, Mn, Zn, Ga, V). *Dalton Trans.* **2017**, *46*, 5352-62.
(21) Liu, L.; Guo, H.; Zhou, M.; Wei, Q.; Yang, Z.; Shu, H.; Yang, X.; Tan, J.; Yan, Z.; Wang, X. A Comparison Among $FeF_3\cdot 3H_2O$, $FeF_3\cdot 0.33H_2O$ and FeF_3 Cathode Materials for Lithium Ion Batteries: Structural, Electrochemical, and Mechanism Studies. *J. Power Sources* **2013**, *238*, 501-15.
(22) Yakubovich, O.; Urusov, V.; Massa, W.; Frenzen, G.; Babel, D. Structure of $Na_2Fe_2F_7$ and structural relations in the family of weberites $Na_2M^{II}M^{III}F_7$. *Z. Anorg. Allg. Chem* **1993**, *619*, 1909-19.
(23) Ramirez, A. P. Strongly Geometrically Frustrated Magnets. *Annu. Rev. Mater. Sci.* **1994**, *24*, 453-80.
(24) Greedan, J. E. Geometrically Frustrated Magnetic Materials. *J. Mater. Chem.* **2001**, *11*, 37-53.
(25) Moessner, R. Magnets with Strong Geometric Frustration. *Can. J. Phys.* **2001**, *79*, 1283-94.
(26) Aczel, A. A.; Bugaris, D. E.; Li, L.; Yan, J.-Q.; de la Cruz, C.; zur Loye, H.-C.; Nagler, S. E. Frustration by Competing Interactions in the Highly Distorted Double Perovskites $La_2NaB'O_6$(B′=Ru, Os). *Phys. Rev. B* **2013**, *87*, 014435.
(27) Balents, L. Spin Liquids in Frustrated Magnets. *Nature* **2010**, *464*, 199-208.
(28) Harrison, A. First Catch Your Hare: The Design and Synthesis of Frustrated Magnets. *J. Condens. Matter Phys.* **2004**, *16*, S553-72.
(29) Kageyama, H.; Hayashi, K.; Maeda, K.; Attfield, J. P.; Hiroi, Z.; Rondinelli, J. M.; Poeppelmeier, K. R. Expanding Frontiers in Materials Chemistry and Physics with Multiple Anions. *Nat. Commun.* **2018**, *9*, 772.
(30) Lacroix, C.; Mendels, P.; Mila, F. Introduction to Frustrated Magnetism: Materials, Experiments, Theory; Springer Series in Soild State Sciences: Berlin, 2011; pp 131-52.
(31) Eyvazov, A. B.; Dusad, R.; Munsie, T. J. S.; Dabkowska, H. A.; Luke, G. M.; Kassner, E. R.; Davis, J. C. S.; Eyal, A. Common Glass-forming Spin-liquid State in the Pyrochlore Magnets $Dy_2Ti_2O_7$ and $Ho_2Ti_2O_7$. *Phys. Rev. B* **2018**, *98*, 214430.
(32) Frandsen, B. A.; Ross, K. A.; Krizan, J. W.; Nilsen, G. J.; Wildes, A. R.; Cava, R. J.; Birgeneau, R. J.; Billinge, S. J. L. Real-Space Investigation of Short-Range Magnetic Correlations in Fluoride Pyrochlores $NaCaCo_2F_7$ and $NaSrCo_2F_7$ with Magnetic Pair Distribution Function Analysis. *Phys. Rev. Mater.* **2017**, *1*, 074412.
(33) Krizan, J. W.; Cava, R. J. $NaSrCo_2F_7$, A Co^{2+} Pyrochlore Antiferromagnet. *J. Condens. Matter Phys.* **2015**, *27*, 296002.
(34) Lemoine, K.; Moury, R.; Durand, E.; Dompablo, E. A.-d.; Morán, E.; Leblanc, M.; Hémon-Ribaud, A.; Grenèche, J.-M.; Galven, C.; Gunes, V.; Lhoste, J.; Maisonneuve, V. First

Mixed-Metal Fluoride Pyrochlores Obtained by Topotactic Oxidation of Ammonium Fluorides under F_2 Gas. *Cryst. Growth Des.* **2021**, *21*, 935-45.
(35) Atwood, J. L. Kagomé lattice: A Molecular Toolkit for Magnetism. *Nat. Mater.* **2002**, *1*, 91-2.
(36) Chi, Y.; Xu, J.; Xue, H. G.; Zhang, Y.; Chen, X.; Whangbo, M. H.; Guo, S. P.; Deng, S. Triple-Kagomé-Layer Slabs of Mixed-Valence Rare-Earth Ions Exhibiting Quantum Spin Liquid Behaviors: Synthesis and Characterization of $Eu_9MgS_2B_{20}O_{41}$. *J. Am. Chem. Soc.* **2019**, *141*, 9533-6.
(37) Helton, J. S.; Matan, K.; Shores, M. P.; Nytko, E. A.; Bartlett, B. M.; Yoshida, Y.; Takano, Y.; Suslov, A.; Qiu, Y.; Chung, J. H.; Nocera, D. G.; Lee, Y. S. Spin Dynamics of the Spin-1/2 Kagome Lattice Antiferromagnet $ZnCu_3(OH)_6Cl_2$. *Phys. Rev. Lett.* **2007**, *98*, 107204.
(38) Jiang, N.; Ramanathan, A.; Bacsa, J.; La Pierre, H. S. Synthesis of a d^1-Titanium Fluoride Kagome Lattice Antiferromagnet. *Nat. Chem.* **2020**, *12*, 691-6.
(39) Lee, P. A. Physics. An End to the Drought of Quantum Spin Liquids. *Science* **2008**, *321*, 1306-7.
(40) Mendels, P.; Olariu, A.; Bert, F.; Bono, D.; Limot, L.; Collin, G.; Ueland, B.; Schiffer, P.; Cava, R. J.; Blanchard, N.; Duc, F.; Trombe, J. C. Spin Dynamics in Frustrated Magnets: from Edge- to Corner-Sharing Geometries. *J. Condens. Matter Phys.* **2007**, *19*, 145224.
(41) Yan, S.; Huse, D. A.; White, S. R. Spin-liquid Ground State of the S = 1/2 Kagome Heisenberg Antiferromagnet. *Science* **2011**, *332*, 1173-6.
(42) Zhang, B.; Baker, P. J.; Zhang, Y.; Wang, D.; Wang, Z.; Su, S.; Zhu, D.; Pratt, F. L. Quantum Spin Liquid from a Three-Dimensional Copper-Oxalate Framework. *J. Am. Chem. Soc* **2018**, *140*, 122-5.
(43) Au, Y. S.; Fu, W. T.; IJdo, D. J. W. Crystal Structure of $Ca_2Ln_3Sb_3O_{14}$ (Ln=La, Pr, Nd and Y): A Novel Variant of Weberite. *J. Solid State Chem.* **2007**, *180*, 3166-71.
(44) Caramanian, A.; Souron, J.-P.; Gredin, P.; de Kozak, A. The Crystal Structure of the Weberite Na_2MgInF_7. *J. Solid State Chem.* **2001**, *159*, 234-8.
(45) Giuseppetti, G.; Tadini, C. Re-examination of the Crystal Structure of Weberite. *Tschermaks Petr. Mitt.* **1978**, *25*, 57-62.
(46) Ruchaud, N.; Grannec, J.; Gravereau, P.; Nunez, P.; Tressaud, A.; Massa, W.; Frenzen, G.; Babel, D. Copper Weberites: Crystal Structure and Magnetic Investigation of Na_2CuGaF_7 and Na_2CuInF_7. *Z. Anorg. Allg. Chem* **1992**, *610*, 67-74.
(47) Hall, W.; Kim, S.; Zubieta, J.; Walton, E. G.; Brown, D. B. Structure of a Mixed-Valence Iron Fluoride, $Fe_2F_5.2H_2O$. *Inorg. Chem.* **1977**, *16*, 1884-7.
(48) Weil, M.; Werner, F. The Thermal Dehydration of Magnesium Aluminum Pentafluoride Dihydrate: Crystal Structures of $MgAlF_5(H_2O)_2$ and $MgAlF_5$. *Monatshefte fuer Chemie* **2001**, *132*, 769-77.
(49) Clark, L.; Albino, M.; Pimenta, V.; Lhoste, J.; da Silva, I.; Payen, C.; Grenèche, J. M.; Maisonneuve, V.; Lightfoot, P.; Leblanc, M. Strong Magnetic Exchange and Frustrated Ferrimagnetic Order in a Weberite-type Inorganic-Organic Hybrid Fluoride. *Philos. Trans. A Math. Phys. Eng. Sci.* **2019**, *377*, 20180224.
(50) Greneche, J. M.; Linares, J.; Varret, F. High-Field Mossbauer-Spectroscopy Applied to Paramagnetic Compounds as a Method of Selcective Susceptibility Measurement. *J. Phys.-Condes. Matter* **1990**, *2*, 4243-51.

(51) Imbert, P.; Jehanno, G.; Macheteau, Y.; Varret, F. Mössbauer Effect Study of $Fe_2F_5(H_2O)_2$. *J. phys. (Paris)* **1976**, *37*, 969-72.
(52) Lemoine, K.; Zhang, L.; Dambournet, D.; Grenèche, J.-M.; Hémon-Ribaud, A.; Leblanc, M.; Borkiewicz, O. J.; Tarascon, J.-M.; Maisonneuve, V.; Lhoste, J. Synthesis by Thermal Decomposition of Two Iron Hydroxyfluorides: Structural Effects of Li Insertion. *Chem. Mater.* **2019**, *31*, 4246-57.
(53) Ayer, G. B.; Klepov, V. V.; Pace, K. A.; zur Loye, H.-C. Quaternary Cerium(IV) Containing Fluorides Exhibiting Ce_3F_{16} Sheets and Ce_6F_{30} Frameworks. *Dalton Trans.* **2020**, *49*, 5898-905.
(54) Ayer, G. B.; Klepov, V. V.; Smith, M. D.; zur Loye, H.-C. Mild Hydrothermal Synthesis of the Complex Hafnium-Containing Fluorides $Cs_2[M(H_2O)_6][Hf_2F_{12}]$ (M = Ni, Co, Zn), $CuHfF_6(H_2O)_4$, and $Cs_2Hf_3Mn_3F_{20}$ Based on HfF_7 and HfF_6 Coordination Polyhedra. *Inorg. Chem.* **2019**, *58*, 13049-57.
(55) Felder, J.; Yeon, J.; Smith, M.; zur Loye, H.-C. Application of a Mild Hydrothermal Method to the Synthesis of Mixed Transition-Metal(II)/Uranium(IV) Fluorides. *Inorg. Chem. Front* **2017**, *4*, 368-77.
(56) Felder, J. B.; Smith, M. D.; Sefat, A.; zur Loye, H.-C. Magnetic and Thermal Behavior of a Family of Compositionally Related Zero-Dimensional Fluorides. *Solid State Sci.* **2018**, *81*, 19-25.
(57) Keerthisinghe, N.; Klepov, V. V.; Zhang, E.; Smith, M. D.; Egodawatte, S.; Foulger, S. H.; zur Loye, H.-C. Hydrothermal Synthesis and Properties of $M^{II}M^{III}F_5(H_2O)_7$ (M^{II}= Co^{2+} and Ni^{2+}, M^{III}= Mn^{3+}, Ga^{3+}, and In^{3+}). *Solid State Sci.* **2020**, *108*, 106374.
(58) Klepov, V. V.; Felder, J. B.; zur Loye, H.-C. Synthetic Strategies for the Synthesis of Ternary Uranium(IV) and Thorium(IV) Fluorides. *Inorg. Chem.* **2018**, *57*, 5597-606.
(59) Klepov, V. V.; Pace, K. A.; Calder, S.; Felder, J. B.; Loye, H. Z. 3d-Metal Induced Magnetic Ordering on U(IV) Atoms as a Route toward U(IV) Magnetic Materials. *J. Am. Chem. Soc.* **2019**, *141*, 3838-42.
(60) APEX3 Version 2019.1-0 and SAINT+ Version 8.40A. **2019**.
(61) Krause, L.; Herbst-Irmer, R.; Sheldrick, G. M.; Stalke, D. Comparison of Silver and Molybdenum Microfocus X-ray Sources for Single-Crystal Structure Determination. *J. Appl. Crystallogr.* **2015**, *48*, 3-10.
(62) Sheldrick, G. M. SHELXT– Integrated Space-Group and Crystal-Structure Determination. *Acta Cryst. A* **2015**, *71*, 3-8.
(63) Dolomanov, O. V.; Bourhis, L. J.; Gildea, R. J.; Howard, J. A. K.; Puschmann, H. OLEX2: A Complete Structure Solution, Refinement and Analysis Program. *J. Appl. Crystallogr.* **2009**, *42*, 339-41.
(64) Hübschle, C. B.; Sheldrick, G. M.; Dittrich, B. ShelXle: A Qt Graphical User Interface for SHELXL. *J. Appl. Crystallogr.* **2011**, *44*, 1281-4.
(65) Kubelka, P. New Contributions to the Optics of Intensely Light-Scattering Materials Part I. *J. Opt. Soc. Am.* **1948**, *38*, 448.
(66) Morrison, G.; zur Loye, H.-C. Simple Correction for the Sample Shape and Radial Offset effects on SQUID Magnetometers: Magnetic Measurements on Ln_2O_3 (Ln=Gd, Dy, Er) Standards. *J. Solid State Chem.* **2015**, *221*, 334-7.
(67) Gallagher, K. J.; Ottaway, M. R. Mixed-Metal Fluoride Hydrates and Their Thermal-Decomposition Products: An Investigation by X-ray, Mössbauer, and Thermal Analysis. *J. Chem. Soc., Dalton Trans.* **1977**, 2212-9.

(68) Hill, H. A. O.; Day, P.; Krogmann, K. Physical Methods in Advanced Inorganic Chemistry. *Angew. Chem.* **1969**, *81*, 267-8.
(69) Tanabe, Y.; Sugano, S. On the Absorption Spectra of Complex Ions I. *J. Phys. Soc. Jpn* **1954**, *9*, 753-66.
(70) Tanabe, Y.; Sugano, S. On the Absorption Spectra of Complex Ions II. *J. Phys. Soc. Jpn* **1954**, *9*, 766-79.
(71) Tanabe, Y.; Sugano, S. On the Absorption Spectra of Complex Ions, III The Calculation of the Crystalline Field Strength. *J. Phys. Soc. Jpn* **1956**, *11*, 864-77.
(72) Greenwood, N. N.; Earnshaw, A. Coordination and Organometallic Compounds. **1997**, *Chemisty of Elements*, 905-43.
(73) König, E. The Nephelauxetic Effect Calculation and Accuracy of the Interelectronic Repulsion Parameters I. Cubic High-Spin d^2, d^3, d^7, and d^8 Systems. **1971**, *Structure and Bonding*, 175-212.
(74) Taran, M. N.; Rossman, G. R. Optical Spectra of Co^{2+} in Three Synthetic Silicate Minerals. *Am. Mineral.* **2001**, *86*, 889-95.
(75) Adachi, S. Review—Photoluminescence Properties of Cr^{3+}-Activated Fluoride Phosphors. *ECS J. Solid State Sci. Technol.* **2021**, *10*, 036001.
(76) Kanamori, J. Superexchange interaction and symmetry properties of electron orbitals. *J. Phys. Chem. Solids* **1959**, *10*, 87-98.
(77) Krizan, J. W.; Cava, R. J. $NaCaNi_2F_7$: A Frustrated High-Temperature Pyrochlore Antiferromagnet with S=1Ni^{2+}. *Phys. Rev. B* **2015**, *92*, 014406.
(78) Ross, K. A.; Brown, J. M.; Cava, R. J.; Krizan, J. W.; Nagler, S. E.; Rodriguez-Rivera, J. A.; Stone, M. B. Single-ion Properties of the S_{eff} = 1/2XY Antiferromagnetic Pyrochlores $NaA'Co_2F_7$ (A′ = Ca^{2+}, Sr^{2+}). *Phys. Rev. B* **2017**, *95*, 144414.
(79) Lacorre, P.; Leblanc, M.; Pannetier, J.; Ferey, G. Ordered Magnetic Frustration. *J. Magn. Magn. Mater.* **1991**, *94*, 337-41.

For Table of Content Use Only

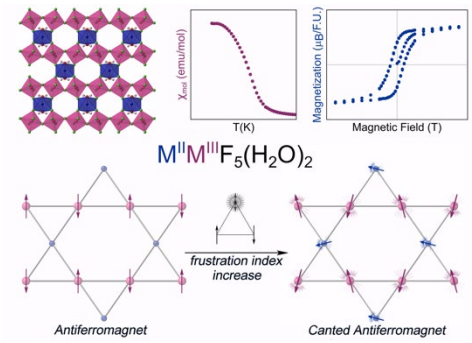

The synthesis and structure of a family of geometrically frustrated $M^{II}M^{III}F_5(H_2O)_2$ mixed–metal fluorides that crystallize with kagome nets is described. Their magnetic properties are discussed.